

High-Speed Vision-Based Flight in Clutter with Safety-Shielded Reinforcement Learning

Jiarui Zhang^{1,2†}, Chengyong Lei^{1,2†}, Chengjiang Dai^{1,2}, Lijie Wang^{1,2},
Zhichao Han^{1,2*}, and Fei Gao^{1,2*}

Abstract—Quadrotor unmanned aerial vehicles (UAVs) are increasingly deployed in complex missions that demand reliable autonomous navigation and robust obstacle avoidance. However, traditional modular pipelines often incur cumulative latency, whereas purely reinforcement learning (RL) approaches typically provide limited formal safety guarantees. To bridge this gap, we propose an end-to-end RL framework augmented with model-based safety mechanisms. We incorporate physical priors in both training and deployment. During training, we design a physics-informed reward structure that provides global navigational guidance. During deployment, we integrate a real-time safety filter that projects the policy outputs onto a provably safe set to enforce strict collision-avoidance constraints. This hybrid architecture reconciles high-speed flight with robust safety assurances. Benchmark evaluations demonstrate that our method outperforms both traditional planners and recent end-to-end obstacle avoidance approaches based on differentiable physics. Extensive experiments demonstrate strong generalization, enabling reliable high-speed navigation in dense clutter and challenging outdoor forest environments at velocities up to 7.5 m/s.

Index Terms—Aerial Robotics; Reinforcement Learning; Collision Avoidance; Safe Control.

I. INTRODUCTION

In recent years, quadrotor Unmanned Aerial Vehicles (UAVs) have been widely adopted in logistics, search and rescue, and exploration missions, owing to their exceptional maneuverability and agility [1], [2]. However, navigation in these unstructured and dynamic environments requires the system to perceive sudden obstacles and execute evasive maneuvers within short time. This creates a fundamental conflict between the demand for high-speed flight and the computational latency required to guarantee rigorous collision avoidance.

Traditional navigation pipelines decompose autonomy into sequential perception, planning, and control modules, achieving reliable performance through explicit algorithmic structures and well-established safety margins [3]–[5]. However, this modular design inevitably incurs cumulative latency, as perception updates, global replanning, and trajectory optimization are repeatedly executed in a closed loop, leading to delayed reactions in rapidly changing environments [6]. Moreover, planning in densely cluttered spaces often requires high-dimensional search or optimization, causing computa-

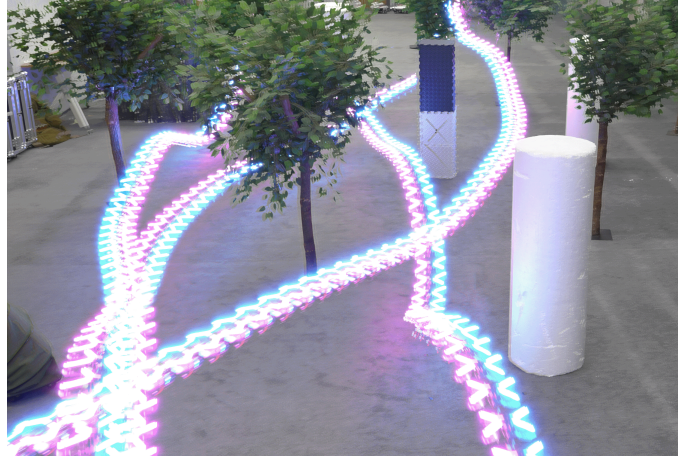


Fig. 1: Snapshot of real-world indoor flight experiments. Flight trajectories recorded via long-exposure photography demonstrate the UAV's agile maneuvering capabilities during high-speed traversal between trees and artificial obstacles.

tional costs to scale poorly with environmental complexity and limiting real-time performance at high flight speeds.

In contrast, learning-based navigation has emerged as an attractive alternative by directly mapping sensory observations to control commands [7]–[11]. Such end-to-end policies significantly reduce processing latency and have demonstrated superior agility in high-speed flight scenarios compared to modular pipelines [12]. Despite these advantages, purely learning-based approaches typically lack theoretical safety guarantees and are vulnerable to out-of-distribution generalization failures, which fundamentally constrain their reliability in safety-critical applications.

To address the lack of formal safety guarantees in purely end-to-end navigation policies while preserving their agility in complex environments, we propose a hybrid navigation framework that tightly couples reinforcement learning with model-based safety mechanisms. The key idea is to exploit the low-latency and expressive power of end-to-end policies for high-speed maneuvering, while enforcing safety through explicit physical constraints. During training, we incorporate model-based priors into the learning process by shaping the reward with global path guidance and safety-related constraints, encouraging the policy to acquire navigation behaviors that are both efficient and risk-aware. During deployment, we further introduce a real-time safety correction module based on high-order control barrier functions, which projects policy outputs onto a provably safe set to guarantee collision avoidance under

†These authors contributed equally to this work.

*Corresponding authors: Zhichao Han and Fei Gao

¹State Key Laboratory of Industrial Control Technology, Zhejiang University, Hangzhou 310027, China.

²Differential Robotics, Hangzhou 311121, China.

E-mail: {jrzrzz, fgaoaa}@zju.edu.cn

unforeseen disturbances and distribution shifts. In addition, we employ robust sim-to-real transfer strategies to ensure consistent performance on real quadrotor platforms.

Our main contributions are summarized as follows:

- 1) A training-time safety-aware navigation framework that integrates global path structure and local collision avoidance into end-to-end reinforcement learning. The proposed approach alleviates local minima in Euclidean distance objectives and enables more foresighted navigation behaviors in cluttered environments.
- 2) A safety enforcement mechanism based on control barrier functions, which guarantees collision avoidance by correcting policy outputs in real time. This mechanism complements learning-based agility with formal safety constraints, enabling high-speed flight without sacrificing reliability under distribution shifts.
- 3) A comprehensive experimental validation across simulation and real-world platforms. Extensive benchmarks demonstrate superior performance over both traditional planners and learning-based baselines, while real-world experiments validate robust sim-to-real transfer and agile navigation in densely cluttered environments.

II. RELATED WORK

A. Modular Navigation for UAV

Traditional optimization-based navigation methods typically rely on explicit 3D environmental representations constructed from depth measurements and manually derived safety constraints [3], [13], [14]. Hard-constrained approaches, for example, decouple planning into extracting a Safe Flight Corridor(SFC)-represented by cubes, spheres, or polyhedrons and subsequently generating trajectories via convex optimization [15]. While ensuring global optimality within the corridor, these methods often depend on heuristic time allocation strategies, which can degrade trajectory quality and lead to conservative dynamic constraints that limit agility.

Conversely, soft-constrained methods, such as those utilizing Euclidean Signed Distance Fields (ESDF), formulate navigation as a joint planning and control problem, leveraging gradient information to efficiently converge upon feasible trajectories within continuous space. However, maintaining real-time ESDF imposes substantial computational overhead on onboard processors due to the expensive calculation of line integrals along the trajectory, necessitating a difficult trade-off between mapping precision and update frequency. To mitigate this, the Ego-Planner [14] circumvents explicit ESDF construction by iteratively generating safe guidance paths to provide obstacle avoidance gradients. Nevertheless, such gradient-based methods lack theoretical convergence guarantees and remain susceptible to entrapment in unsafe local minima within complex, non-convex environments. Furthermore, the cascading architecture of these multi-module systems introduces significant parameter complexity and cumulative latency, which often leads to state estimation instability during high-speed flight, thereby limiting their robustness in dynamic scenarios.

B. Learning-Based Methods

Recent studies underscore the immense potential of learning-based methodologies, which obviate the need for dense mapping or explicit environmental modeling. By directly mapping sensory observations to control commands, these approaches circumvent the cumulative latency and computational burden associated with modular trajectory optimization, demonstrating impressive maneuverability [16], [17]. NavRL [18] introduces a PPO-based framework that enables safe and reactive navigation in dynamic environments with moving obstacles, achieving low collision rates through careful reward design and curriculum training. Similarly, approaches such as [10] and [19] proposes an RL pipeline that dynamically adapts flight speed based on environmental clutter, striking an effective balance between success rate and agility in unknown cluttered spaces. Furthermore, emerging research has leveraged differentiable simulators and optimization-embedded networks to refine controller performance. In a hybrid direction, optimization-embedded networks [20] integrate traditional trajectory parameterization with neural networks to generate dynamically feasible trajectories directly from depth inputs, bridging perception and planning while ensuring kinematic constraints without explicit mapping.

While these learning-based approaches have propelled UAV agility to new heights, their inherent lack of theoretical completeness often compromises reliability in safety-critical scenarios. To address this limitation, our proposed pipeline builds upon a PPO training framework but explicitly integrates model-based designs [21]. This hybrid strategy aims to bridge the gap between agility and safety, endowing the learned policy with enhanced robustness and mathematically grounded guarantees.

III. METHODOLOGY

A. Problem Formulation

We formulate the real-time interaction between the simulated UAV and its complex, dynamic surroundings as a Markov Decision Process (MDP). Formally, the MDP is defined as the tuple $(\mathcal{S}, \mathcal{A}, \mathcal{P}, \mathcal{R}, \gamma)$, where \mathcal{S} denotes the state space, \mathcal{A} the action space, $\mathcal{P} : \mathcal{S} \times \mathcal{A} \times \mathcal{S} \rightarrow [0, 1]$ the state-transition probability, $\mathcal{R} : \mathcal{S} \times \mathcal{A} \rightarrow \mathbb{R}$ the reward function, and $\gamma \in [0, 1]$ the discount factor. Detailed descriptions of the observation space, action space, and reward design employed in our framework are provided in the subsequent subsections III-A1, III-A2 and III-A3.

1) *Observation Space*: The training loop initiates by acquiring the current observation of the UAV state. The observation input to our policy network is structured as a multi-modal composite vector \mathbf{o}_t , integrating both exteroceptive environmental perception and the proprioceptive state of the UAV. Specifically, the observation is defined as:

$$\mathbf{o}_t = [\mathbf{D}_t, \mathbf{v}_t, \mathbf{R}_t, \mathbf{a}_{t-1}, \mathbf{d}_t^{xy}, h_t^{\text{self}}, h_t^{\text{goal}}], \quad (1)$$

where the components are detailed as follows:

- $\mathbf{D}_t \in \mathbb{R}^{100 \times 60}$: the depth image captured by the onboard camera.

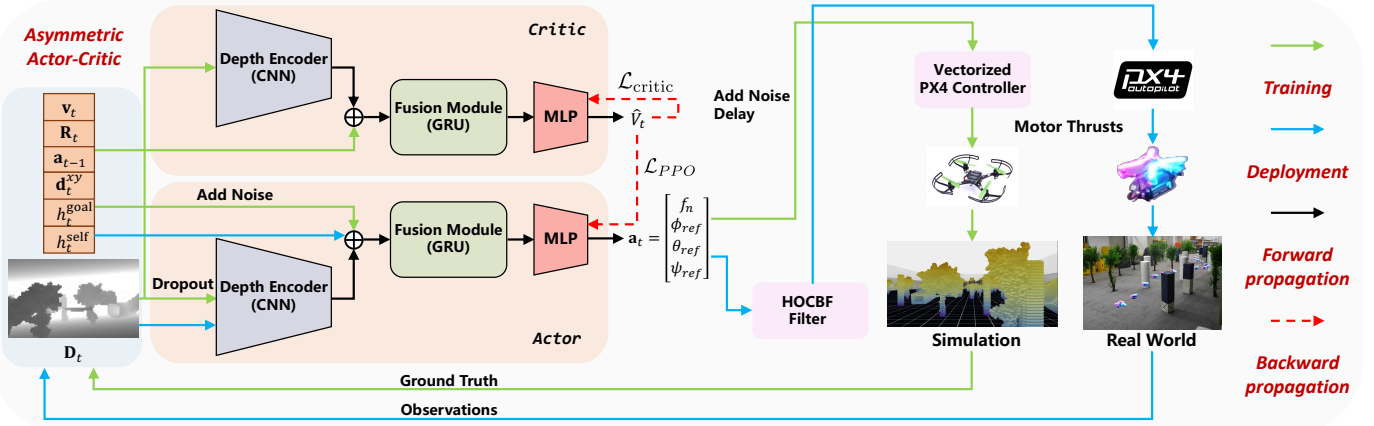


Fig. 2: **Network architecture and control pipeline.** An asymmetric actor-critic fuses a depth image (CNN) and proprioceptive states via a GRU. The actor outputs attitude references and normalized thrust, which are tracked by a PX4 controller. During training, domain randomization (dropout/noise/delay) improves robustness; during deployment, a real-time HO-CBF filter refines the raw command to enforce safety constraints.

- $\mathbf{v}_t \in \mathbb{R}^3$: the linear velocity vector expressed in the body coordinate frame.
- $\mathbf{R}_t \in SO(3)$: the rotation matrix representing the current attitude of the UAV.
- \mathbf{a}_{t-1} : the action executed at the previous time step, comprising roll, pitch, yaw, and total thrust. This historical action serves as a reference to ensure control smoothness.
- $\mathbf{d}_t^{xy} = [\Delta x, \Delta y]^\top$: the normalized horizontal position difference relative to the target.
- h_t^{self} and h_t^{goal} : the current altitude of the UAV and the target altitude, respectively.

2) *Action Space*: The policy network processes the aforementioned observations and outputs a four-dimensional action vector $\mathbf{a}_t \in \mathbb{R}^4$, defined as:

$$\mathbf{a}_t = [f_n, \phi_{\text{ref}}, \theta_{\text{ref}}, \psi_{\text{ref}}]^\top, \quad (2)$$

this vector consists of the mass-normalized collective thrust f_n and the desired attitude angles (roll ϕ_{ref} , pitch θ_{ref} , and yaw ψ_{ref}). The control commands are updated at a fixed frequency of 100 Hz to guarantee real-time responsiveness. Subsequently, the low-level onboard flight controller solves for the required rotational speeds of individual motors to achieve precise tracking of these high-level commands.

To ensure operational safety, real-world UAVs typically enforce bounded attitude commands to prevent aggressive maneuvers that may lead to loss of control. Accordingly, instead of issuing low-level control inputs such as direct motor speeds, we adopt attitude-level control commands as the policy output. This higher-level control abstraction significantly reduces the sim-to-real gap by aligning the action space in simulation with practical flight controllers used on physical platforms, thereby improving the robustness of sim-to-real transfer [22].

3) *Reward Function Design*: In this work, the overall reward r_t is defined as a weighted sum of distinct components:

$$\begin{aligned} r_t = & \alpha_1 r_{\text{navigation}} + \alpha_2 r_{\text{safety}} + \alpha_3 r_{\text{smooth}} \\ & + \alpha_4 r_{\text{collision}} + \alpha_5 r_{\text{success}} \\ & + \alpha_6 r_{\text{speed}} + \alpha_7 r_{\text{height}}. \end{aligned} \quad (3)$$

Specifically, the total reward is composed of navigation guidance, safety regulation, control regularization, and terminal signals. The model-based components $r_{\text{navigation}}$ and r_{safety} , detailed in Section III-C, provide global path guidance and safety-aware shaping during training. To ensure executable and stable control behavior, the smoothness term r_{smooth} penalizes both large control magnitudes and abrupt changes between consecutive actions, encouraging dynamically feasible and smooth trajectories. Terminal rewards $r_{\text{collision}}$ and r_{success} are applied upon collision events and successful task completion, respectively, providing clear episodic feedback. In addition, auxiliary terms, r_{speed} and r_{height} softly constrain the UAV's velocity and altitude within predefined safety limits, preventing unrealistic or unsafe behaviors during exploration. The overall reward is formulated as a weighted sum, where α_i denotes the coefficient of the i -th term. These weights are empirically tuned to balance safety, agility, and task completion during training.

B. Network Architecture

We employ the Proximal Policy Optimization (PPO) algorithm within an asymmetric actor-critic framework. This architecture leverages a privileged learning paradigm: while the critic network is trained on noise-free ground truth states to facilitate stable value estimation, the actor network operates solely on noisy observations to ensure robust deployment under real-world uncertainties.

The complete network structure is illustrated in Fig. 2. To effectively process multimodal inputs, the actor utilizes a heterogeneous neural architecture. The visual stream processes a 100×60 depth image via a Convolutional Neural Network (CNN) composed of sequential convolutional, activation (ReLU), and pooling layers, extracting a compact visual feature vector f_{CNN} that encodes spatial geometry. We directly concatenate this visual embedding with the raw proprioceptive observations, which consist of the quadrotor's linear velocity, rotation matrix, previous action, and goal-relative displacement. This unified vector is subsequently fed

into a Gated Recurrent Unit (GRU). The GRU maintains a temporal hidden state h_t to aggregate historical context, enabling the policy to mitigate partial observability and smooth sensor noise over time. Finally, the GRU output is passed to a Multi-Layer Perceptron (MLP) head, which predicts the Gaussian distribution parameters for the continuous action command \mathbf{a}_t .

C. Model-based Reward Shaping

We begin by formulating the navigation reward $r_{\text{navigation}}$. Conventional distance-based rewards typically rely on Euclidean distance to shape the policy. Although this offers dense feedback, it often leads to convergence failures in non-convex environments. The agent, driven by the greedy minimization of Euclidean distance, is prone to the local minima trap, failing to navigate around complex obstacles. To overcome this, we propose a geodesic-guided reward mechanism, as outlined in Algorithm 1. Instead of Euclidean distance, we utilize a precomputed cost map derived from Dijkstra algorithm, which represents the true shortest-path distance considering obstacles. This map serves as a dense potential field during training. By applying trilinear interpolation, we extract continuous cost values \mathbf{V}_t at the real-time coordinates of the UAV. The reward is then formulated based on the progress δ along this potential field. This approach provides the agent with global geometric awareness, effectively decomposing the long-horizon task into accessible local subgoals and guiding the UAV out of local minima.

Let Φ_g denote the precomputed geodesic distance field (via Dijkstra) for a given scene g . The navigation reward $r_{\text{navigation},t}$ at time step t is defined as the clipped progress made along this potential field:

$$r_{\text{navigation},t} = \lambda \cdot \text{clamp}(\underbrace{\text{Interp}(\Phi_g, \mathbf{p}_{t-1}) - \text{Interp}(\Phi_g, \mathbf{p}_t)}_{\mathbf{v}_{t-1}}, -C, C), \quad (4)$$

where $\text{Interp}(\cdot)$ represents the trilinear interpolation function that maps the continuous UAV position \mathbf{p} to the discrete Dijkstra cost grid, λ is a scaling factor, and the clamp function ensures numerical stability by bounding the reward within $[-C, C]$.

Algorithm 1 Dijkstra-Based Navigation Reward

Require: Set of Dijkstra value gridmaps $\{\Phi_g\}_{g \in \mathcal{G}}$; current states \mathbf{x}_t ; previous states \mathbf{x}_{t-1} ; clipping bound C ; scaling factor λ

Ensure: Navigation reward vector \mathbf{r}_{dijk}

- 1: **for** each scene $g \in \mathcal{G}$ **do**
- 2: $\mathcal{I}_g \leftarrow \{id \mid \text{env}_{id} \in \text{scene } g\}$
- 3: $\mathbf{V}_t \leftarrow \text{TrilinearInterpolation}(\Phi_g, \mathbf{x}_t[\mathcal{I}_g])$
- 4: $\mathbf{V}_{t-1} \leftarrow \text{TrilinearInterpolation}(\Phi_g, \mathbf{x}_{t-1}[\mathcal{I}_g])$
- 5: $\delta \leftarrow \mathbf{V}_{t-1} - \mathbf{V}_t$
- 6: $\delta \leftarrow \text{clamp}(\delta, -C, C)$
- 7: $\mathbf{r}_{dijk}[\mathcal{I}_g] \leftarrow \lambda \cdot \delta$
- 8: **end for**
- 9: **return** \mathbf{r}_{dijk}

To enhance flight safety, we incorporate a shaping reward based on Control Barrier Function [23]–[25]. We first construct

a ESDF from the obstacle map, where $d(\mathbf{x})$ denotes the minimum distance from position \mathbf{x} to the nearest obstacle. The barrier function is defined as $h(\mathbf{x}) = d(\mathbf{x}) - d_{\text{safe}}$, where d_{safe} is a prescribed safety margin. According to CBF theory, safety is guaranteed if the forward-invariance condition $h(\mathbf{x}) + \gamma h(\mathbf{x}) \geq 0$ is satisfied. Instead of enforcing this constraint explicitly, we encode the violation of this condition into the reward function. Specifically, at each timestep t , we compute the time derivative of the barrier function as $\dot{h}(\mathbf{x}_t) = \nabla d(\mathbf{x}_t) \cdot \mathbf{v}_t$, utilizing the gradient of the ESDF and the current velocity vector of the UAV. The safety reward r_{safety} is then formulated as:

$$r_{\text{safety}} = \text{clip}(\dot{h}(\mathbf{x}_t) + \gamma h(\mathbf{x}_t), \delta_{\text{min}}, 0), \quad (5)$$

where γ is the CBF coefficient. We impose a clipping threshold $\delta_{\text{min}} = -2.0$ on the safety reward. This lower bound prevents unbounded penalties from destabilizing the value function approximation and causing gradient explosion, thereby ensuring numerical stability during training. This mechanism encourages the UAV to proactively align its velocity with the ESDF gradient to satisfy the barrier condition, effectively anticipating and avoiding collision risks.

D. HOCBF-based Correction Loop

Since reward shaping only acts as a soft incentive rather than a hard constraint, the agent can still suffer severe failures. To provide theoretical safety guarantees during real-world deployment, we integrate a safety filter based on High-Order Control Barrier Functions (HOCBF) [26]. This optimization layer minimally deviates from the raw reference action of the policy \mathbf{a}_{raw} to strictly satisfy safety constraints. We formulate this as a Quadratic Program (QP):

$$\mathbf{a}^* = \arg \min_{\mathbf{a}} \frac{1}{2} |\mathbf{a} - \mathbf{a}_{\text{raw}}|^2 \quad \text{s.t.} \quad \mathcal{C}(\mathbf{r}_t, \mathbf{a}) \geq 0. \quad (6)$$

For an obstacle i , we define the candidate barrier function $h_i(\mathbf{r}_t) = \|\mathbf{r}_t\|^2 - r_{\text{safe}}^2$, where \mathbf{r}_t denotes the relative position vector extending from the UAV to the nearest obstacle point identified within the local point cloud reconstructed from real-time depth observations and r_{safe} is the safety radius. Considering the second-order nature of quadrotor dynamics, we employ the HOCBF formulation to ensure the forward invariance of the safe set. The associated safety constraint is defined as:

$$\ddot{h}_i(\mathbf{r}_t) + \alpha_1 \dot{h}_i(\mathbf{r}_t) + \alpha_0 h_i(\mathbf{r}_t) \geq 0, \quad (7)$$

where $\alpha_0, \alpha_1 > 0$ are adjustable coefficients. By substituting the time derivatives $\dot{h}_i(\mathbf{r}_t) = 2\mathbf{r}_t \cdot \mathbf{v}_t$ and $\ddot{h}_i(\mathbf{r}_t) = 2\|\mathbf{v}_t\|^2 + 2\mathbf{r}_t \cdot \mathbf{a}_t$, we derive a linear inequality constraint on the control action \mathbf{a} :

$$\underbrace{2\mathbf{r}_t^\top \mathbf{a}_t}_{\mathbf{A}_{\text{cbf}}} \geq \underbrace{-2\|\mathbf{v}_t\|^2 - \alpha_1 \dot{h}_i(\mathbf{r}_t) - \alpha_0 h_i(\mathbf{r}_t)}_{b_{\text{cbf}}}. \quad (8)$$

Here, \mathbf{A}_{cbf} encapsulates the gradient direction for collision avoidance, while b_{cbf} quantifies the minimum required control effort to counteract the inertia of the system and ensure boundary invariance. This linear constraint allows the QP

solver to efficiently compute safe control commands \mathbf{a}^* in real-time, effectively correcting unsafe maneuvers while preserving the intended flight trajectory.

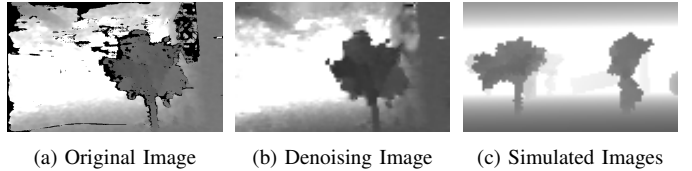
E. Sim-to-Real Transfer

Although the proposed policy achieves fast convergence and high success rates in simulation, discrepancies between simulated and real-world systems can lead to performance degradation during deployment. These discrepancies primarily arise from unmodeled dynamics, including system latency, sensor noise, and actuation uncertainties. To improve robustness and facilitate reliable sim-to-real transfer, we adopt a comprehensive domain randomization strategy during training. To emulate system-level latency commonly observed on physical UAV platforms, the real-time control output is replaced by the average action over a historical window of duration δ_t , where the delay is randomly sampled from the range of 60-80 ms. In addition, we employ an asymmetric noise injection scheme to stabilize learning while enhancing robustness. Specifically, the critic network is provided with privileged, noise-free ground truth states to ensure accurate value estimation, whereas the actor network operates on noisy observations. Sensor noise is modeled using additive Gaussian noise for position, multiplicative scaling noise for linear velocity, and rotational perturbations for attitude measurements. Additionally, to account for perception and actuation uncertainties, we randomly apply pixel dropouts to depth images and inject uniform noise ($\pm 10\%$) into the control actions during training. Together, these randomization strategies expose the policy to a wide range of realistic disturbances, improving its robustness and generalization performance when transferred to real-world UAV platforms.

Furthermore, to bridge the perceptual domain gap arising from the discrepancy between ideal simulated depth images and real-world sensor data, which is frequently degraded by artifacts, signal loss, and distortion during high-speed maneuvers, we implement a robust sim-to-real strategy. During the simulation phase, we introduce a randomized pixel dropout mechanism designed to emulate error distributions observed during high-speed flight. By randomly saturating a subset of pixels, we mimic characteristic signal loss and distortion, compelling the policy to learn feature representations that are invariant to sparse or corrupted depth information. Complementarily, during real-world deployment, we apply a Navier-Stokes-based inpainting algorithm to restore spatial consistency [27]. As illustrated in Fig. 3, by leveraging gradients from surrounding pixels to interpolate depth voids, this technique effectively fills large missing regions while preserving strong edges and obstacle boundaries. By minimizing the distributional shift between real-world inputs and the simulated observation space, this pipeline ensures robust policy transfer and consistent performance in physical environments.

IV. EXPERIMENTS

To validate the efficacy of the proposed framework, we first evaluate training performance across various reward configurations. Subsequently, ablation studies are conducted by



(a) Original Image (b) Denoising Image (c) Simulated Images

Fig. 3: Visualization of depth observations. (a) Raw depth image captured by an Intel RealSense D435i camera. (b) Processed image after applying the Navier-Stokes inpainting algorithm. (c) Synthetic depth image generated from the simulated sensor.

deploying the policy in diverse, unseen environments with dimensions of $64 \times 32 \times 3$ m to assess its impact on success rates. Furthermore, we benchmark the proposed method against state-of-the-art approaches, including the planning-based Ego-Planner [14] and the learning-based DiffPhys [11], demonstrating that our method consistently maintains the target velocity setpoint while ensuring rigorous safety. Real-world feasibility is verified through indoor experiments with varying obstacle configurations, compared against Ego-PlannerV2 [5]. Finally, we demonstrate the high-speed navigation capability of the framework in a cluttered outdoor forest, achieving agile flight at speeds up to 7.5 m/s.

A. Simulations

1) *Training Results*: Our framework is trained in Isaac Lab using large-scale parallel simulation, deploying 1,000 quadrotors simultaneously across 16 procedurally generated scenes of increasing difficulty. Each scene consists of randomly distributed geometric obstacles, with obstacle density gradually rising alongside the difficulty level. At the beginning of each episode, the initial position of the drone is uniformly randomized within the free space located before the obstacle field. An episode is considered successful if the drone reaches the goal region, defined as being within a 5-meter radius of the target position.

To investigate the impact of reward shaping on learning efficiency and navigation performance, we compare three reward formulations: (i) Distance, which utilizes the Euclidean distance to the target as the navigation reward; (ii) Dijkstra, which replaces the Euclidean metric with a Dijkstra-based potential value for global guidance; and (iii) Dijkstra + CBF, which augments the Dijkstra reward with an additional CBF-based safety term to penalize proximity to obstacles. The learning curves in Fig. 4a demonstrate that, under identical training conditions, the Dijkstra-based navigation reward substantially accelerates policy learning and achieves a consistently higher success rate than the Distance baseline. Moreover, incorporating the CBF-based safety reward encourages safer exploration and yields further improvements in final performance, achieving the highest success rate among all compared variants.

2) *Ablation Studies*: We assess the individual contributions of the Dijkstra-based navigation reward, the CBF-based safety reward, and the HOCBF safety filter through ablation experiments across eight diverse environments that are explicitly excluded from the training set. These procedurally generate scenes contain randomly distributed geometric primitives with

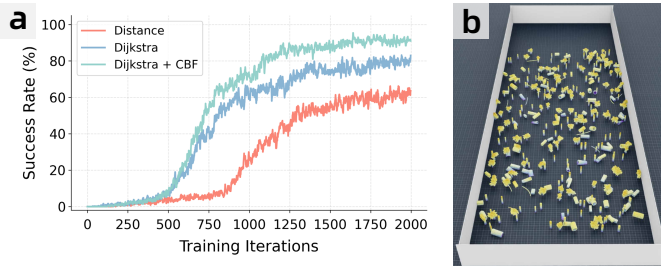


Fig. 4: **Training performance and environment.** (a) Comparative training curves displaying success rates over iterations for different reward configurations. (b) Visualization of a representative training scenario populated with dense obstacles.

complex non-convex topologies. We execute 50 independent trials per scene, with the results summarized in Tab. I. Overall, the results strongly validate our hierarchical design: global guidance ensures reachability, while the hybrid safety mechanism (soft shaping + hard filter) guarantees robustness across the entire speed envelope.

Global guidance for reachability. The Euclidean-distance baseline suffers rapid degradation at higher velocities due to its myopic nature, frequently leading to failure in complex clutter. In contrast, integrating the Dijkstra-based potential field significantly enhances reachability by encoding global topological information, which provides consistent gradients to steer the agent away from local minima (e.g., U-shaped traps). This strategy effectively distills long-horizon planning capabilities into the reactive policy without incurring online search latency. Notably, the slightly superior performance observed at 5m/s compared to 3m/s suggests that moderate forward velocity promotes trajectory smoothness, whereas lower speeds may induce excessive corrective maneuvers or hesitation near complex obstacles.

Necessity of the hybrid safety architecture. Augmenting the policy with a CBF-based safety reward enhances performance in low-to-medium speed regimes by providing crucial guidance that fosters safer exploration. However, under high-dynamic conditions (7 m/s and 9 m/s), the efficacy of this soft reward shaping exhibits a slight decline, as evidenced in Tab. I where the reward-only variant marginally underperforms the Dijkstra-only baseline. This slight degradation is not attributable to excessive conservatism, but rather to the inherent difficulty of learning precise safety boundaries through soft penalties alone; at high velocities, significant system inertia renders safety margins extremely sensitive to control inputs, making it challenging for the RL agent to approximate these stiff constraints solely via reward feedback.

This limitation underscores the critical necessity of our HOCBF safety filter. Unlike the soft reward, which functions as an implicit optimization objective during training, the HOCBF filter acts as a deterministic safeguard during deployment. By solving a real-time QP to project raw commands onto a provably safe set with minimal deviation, the filter effectively compensates for the approximation errors of the neural policy. This hierarchical decoupling allows the RL agent to prioritize efficient global navigation, while the filter manages high-frequency, safety-critical adjustments. Consequently, the full

TABLE I: Results of Ablation Study Across Target Speeds

Configuration	3 m/s		5 m/s		7 m/s		9 m/s	
	SR↑	Vel	SR↑	Vel	SR↑	Vel	SR↑	Vel
Distance	51.75	3.04	35.00	5.16	21.25	7.11	0	-
Dijkstra	62.25	3.02	67.75	5.18	56.25	6.76	43.75	8.36
Dijkstra + CBF	84.50	3.03	94.00	4.99	52.25	6.99	37.25	8.70
Ours (Full)	88.75	3.00	100	4.90	75.0	6.79	47.50	9.00

* SR: Success Rate (%), Vel: Average Velocity (m/s).

TABLE II: Benchmark Comparison of Success Rates Across Target Speed

Method	3 m/s	5 m/s	7 m/s	9 m/s
EGO-Planner [14]	20.0%	0%	0%	0%
Diffphys [11]	75.0%	25.0%	22.5%	17.5%
Ours	87.5%	75.0%	42.5%	25.0%

framework (Dijkstra + CBF + HOCBF) effectively bridges the gap between learning-based agility and model-based safety, yielding superior robustness.

3) *Benchmarks:* We benchmark our proposed framework against two state-of-the-art baselines: the planning-based Ego-Planner [14] and the learning-based DiffPhys [11]. The DiffPhys baseline was implemented with an observation space comprising depth images, target velocity, altitude, and body-frame velocity, utilizing a safety margin of 0.2 m. Experiments were conducted in four challenging test environments (Fig. 5b), categorized into two types: (1) cluttered geometric scenes composed of randomly distributed primitives (e.g., cylinders, ellipsoids, boxes) that induce highly non-convex traversability, similar to the setup in Sec. IV-A2, and (2) procedurally generated obstacle fields based on Perlin noise. For each method, we executed 10 independent trials across varying target speeds, with the aggregate success rates reported in Tab. II.

As detailed in Tab. II, Ego-Planner [14] yields a viable success rate only at the lowest target speed (3 m/s) and fails completely at higher velocities. This performance degradation is characteristic of optimization-based pipelines, where the computational latency of iterative re-planning often exceeds the fast reaction time required for high-speed collision avoidance, leading to unavoidable crashes.

While DiffPhys [11] outperforms Ego-Planner [14] at moderate speeds, it struggles to scale to higher velocities, exhibiting both lower success rates and an inability to track high target setpoints (Fig. 5a). This degradation stems primarily from its predefined heading strategy, which creates a fundamental conflict between agile control and effective perception. During rapid acceleration or deceleration, the substantial body pitch inevitably shifts the limited camera field of view towards the ground or sky, respectively. Lacking the capability for active yaw adaptation to compensate for these visual occlusions, the agent suffers from intermittent loss of environmental awareness. Compounding this perceptual deficit is the lack of explicit safety constraints in both training and deployment. Consequently, the policy is forced to either fly blindly, leading to frequent collisions, or adopt conservative braking behaviors

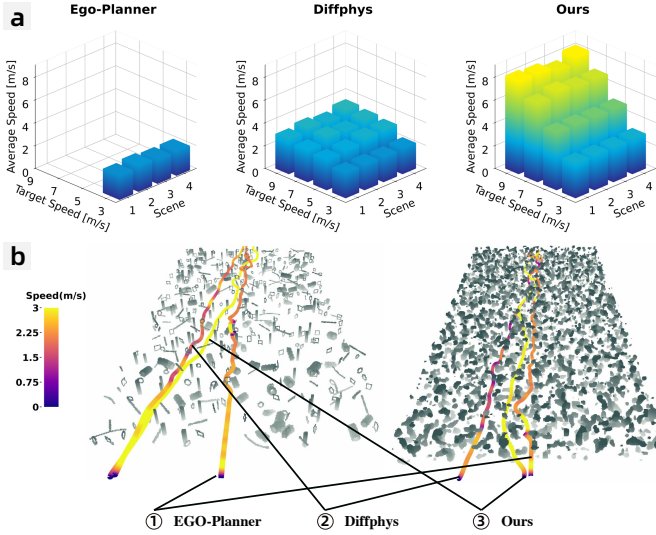


Fig. 5: **Benchmark comparisons against state-of-the-art methods.** (a) Average realized velocity of Ego-Planner [14], DiffPhys [11], and our method across varying target speeds and environmental configurations. (b) Visualization of the resulting flight trajectories generated by each method in geometric clutter (left) and Perlin noise (right) scenarios.

to stabilize visual inputs, thereby severely limiting the realized velocity.

Conversely, our method demonstrates superior safety performance during high-speed flight, consistently achieving higher realized speeds across all environmental configurations (Fig. 5a). By maintaining exceptional success rates throughout the full speed envelope, our approach validates the advantage of combining low-latency learning with model-based safety, successfully bridging the gap between extreme agility and rigorous safety.

B. Real-World Experiments

To further validate the proposed framework, we deployed the trained policy on a physical quadrotor and conducted extensive experiments in both cluttered indoor environments and unstructured outdoor forests. These tests were designed to evaluate the stability of the system and utility under complex conditions and high-speed flight.

We employ Visual-Inertial Odometry (VIO) to acquire 6-DoF pose information, which is subsequently fused with raw Inertial Measurement Unit (IMU) data via an Extended Kalman Filter (EKF) to yield high-frequency proprioceptive state estimates. For environmental perception, raw depth images acquired by an Intel RealSense D435i camera are downsampled to match the simulation resolution. To mitigate sensor noise and artifacts, we apply a Navier–Stokes-based inpainting algorithm, with depth values clipped at 7m. The policy inference executes on an onboard Nvidia Orin NX computer, generating attitude control commands at 100Hz. These commands are transmitted to a PX4 flight controller, which computes the requisite low-level motor speeds.

We construct a cluttered indoor test environment, as shown in Fig. 6. The policy is evaluated using networks trained with target speed constraints of 3 m/s, 5 m/s, and 7 m/s. To

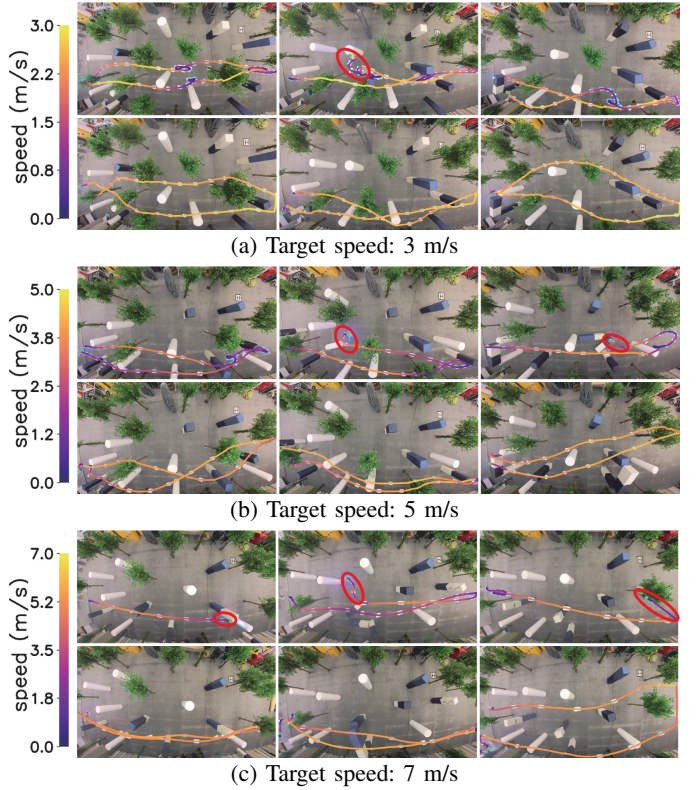


Fig. 6: Snapshots of indoor real-world experiments at varying target speeds. Each subfigure demonstrates three independent trials conducted under distinct obstacle configurations to evaluate robustness. In each panel, the top and bottom rows compare the performance of Ego-Planner (**Top**) and our proposed method (**Bottom**), respectively.

assess generalization capabilities, the quadrotor is tasked with navigating back and forth through a 15 m long obstacle course, with the obstacle layout randomly reconfigured before each flight.

Experimental results demonstrate that our policy executes obstacle avoidance and navigation tasks with an exceptionally high success rate across varying speeds and scene configurations. When compared to the traditional planning algorithm Ego-PlannerV2 [5] under identical conditions, our method exhibits superior performance in terms of both flight stability and maximum achievable velocity. As illustrated in Fig. 6, where red circles denote collision events, Ego-PlannerV2 [5] suffers from a marked increase in failures as the target speed rises. In contrast, our method consistently achieves successful navigation while maintaining an actual velocity that closely tracks the target setpoint for the majority of the trajectory.

In outdoor forest scenarios (Fig. 7), we employ a policy trained with a setup modified only by reducing obstacle density and increasing the target speed limit compared to the original training configuration. The quadrotor successfully achieves stable, high-speed, long-distance obstacle avoidance, maintaining an average velocity of 7 m/s over a distance exceeding 35 m to reach the target.

Such challenging flight missions impose stringent demands on the accuracy and latency of the control system, where even minor errors can lead to catastrophic failures. Capitalizing on the inherent low latency and mapping-free efficiency of the end-to-end architecture, and further integrating dijkstra

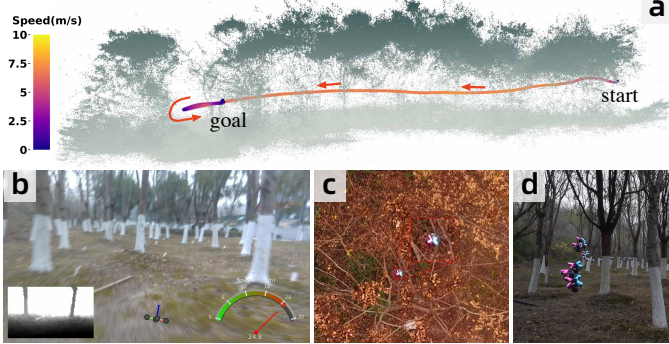


Fig. 7: **Visualization of the outdoor flight experiment.** (a) Global point cloud map overlaid with the executed trajectory and the corresponding realized speed profile. (b) Egocentric observations, including RGB and aligned depth images (Intel RealSense D435i), augmented with real-time attitude and speedometer displays. (c) Top-down view of the environment. (d) Side-view composite image illustrating the sequential flight maneuvers through the dense vegetation.

guidance with safety shielding mechanisms to circumvent local minima and ensure flight safety, our method demonstrated outstanding agility and robustness throughout these experiments. A complete demonstration of these flights is provided in the supplementary video.

V. CONCLUSION

In this paper, we present a hybrid reinforcement learning framework that synergizes model-free policy optimization with model-based physical priors, enabling quadrotors to achieve autonomous high-speed obstacle avoidance. By incorporating physical priors into both training and deployment phases, we establish a robust pipeline: during training, global geometric guidance and safety-aware exploration are utilized to accelerate convergence; during deployment, a real-time filter is integrated to ensure smooth and feasible control. Extensive real-world experiments at velocities up to 7.5 m/s have validated the unprecedented reliability and agility of the system, demonstrating superior sim-to-real transfer capabilities. For future work, we aim to refine this framework to enhance its perception and avoidance capabilities against dynamic agents and fine-scale obstacles. Additionally, we plan to extend the adaptability of our approach to more specific and complex task-oriented scenarios.

REFERENCES

- [1] B. Zhou, Y. Zhang, X. Chen, and F. Gao, “FUEL: Fast uav exploration using incremental frontier structure and hierarchical planning,” *IEEE Robotics and Automation Letters*, vol. 6, no. 2, pp. 779–786, 2021.
- [2] Z. Xu, B. Chen, X. Zhan, Y. Xiu, C. Suzuki, and K. Shimada, “A vision-based autonomous uav inspection framework for unknown tunnel construction sites with dynamic obstacles,” *IEEE Robotics and Automation Letters*, vol. 8, no. 8, pp. 4983–4990, 2023.
- [3] B. Zhou, F. Gao, L. Wang, C. Liu, and S. Shen, “Robust and efficient quadrotor trajectory generation for fast autonomous flight,” *IEEE Robotics and Automation Letters*, vol. 4, no. 4, pp. 3529–3536, 2019.
- [4] F. Gao, L. Wang, B. Zhou, X. Zhou, J. Pan, and S. Shen, “Teach-repeat-replan: A complete and robust system for aggressive flight in complex environments,” *IEEE Transactions on Robotics*, vol. 36, no. 5, pp. 1526–1545, 2020.
- [5] X. Zhou, X. Wen, Z. Wang, Y. Gao, H. Li, Q. Wang, T. Yang, H. Lu, Y. Cao, C. Xu *et al.*, “Swarm of micro flying robots in the wild,” *Science Robotics*, vol. 7, no. 66, p. eabm5954, 2022.
- [6] T. Wu, Y. Chen, T. Chen, G. Zhao, and F. Gao, “Whole-body control through narrow gaps from pixels to action,” *arXiv preprint arXiv:2409.00895*, 2024.
- [7] G. Kahn, P. Abbeel, and S. Levine, “Badgr: An autonomous self-supervised learning-based navigation system,” *IEEE Robotics and Automation Letters*, vol. 6, no. 2, pp. 1312–1319, 2021.
- [8] H. Nguyen, S. H. Fyhn, P. De Petris, and K. Alexis, “Motion primitives-based navigation planning using deep collision prediction,” in *2022 International Conference on Robotics and Automation (ICRA)*. IEEE, 2022, pp. 9660–9667.
- [9] Y. Song, K. Shi, R. Penicka, and D. Scaramuzza, “Learning perception-aware agile flight in cluttered environments,” *arXiv preprint arXiv:2210.01841*, 2022.
- [10] H. Yu, C. De Wagter, and G. C. E. de Croon, “Mavrl: Learn to fly in cluttered environments with varying speed,” *IEEE Robotics and Automation Letters*, 2024.
- [11] Y. Zhang, Y. Hu, Y. Song, D. Zou, and W. Lin, “Learning vision-based agile flight via differentiable physics,” *Nature Machine Intelligence*, pp. 1–13, 2025.
- [12] A. Loquercio, E. Kaufmann, R. Ranftl, M. Müller, V. Koltun, and D. Scaramuzza, “Learning high-speed flight in the wild,” *Science Robotics*, vol. 6, no. 59, p. eabg5810, 2021.
- [13] D. Scaramuzza, M. C. Achtelik, L. Doitsidis, F. Friedrich, E. Kosmatopoulos, A. Martinelli, M. W. Achtelik, M. Chli, S. Chatzichristofis, L. Kneip *et al.*, “Vision-controlled micro flying robots: from system design to autonomous navigation and mapping in gps-denied environments,” *IEEE Robotics & Automation Magazine*, vol. 21, no. 3, pp. 26–40, 2014.
- [14] X. Zhou, Z. Wang, H. Ye, C. Xu, and F. Gao, “Ego-planner: An esdf-free gradient-based local planner for quadrotors,” *IEEE Robotics and Automation Letters*, vol. 6, no. 2, pp. 478–485, 2020.
- [15] S. Liu, M. Waterson, K. Mohta, K. Sun, S. Bhattacharya, C. J. Taylor, and V. Kumar, “Planning dynamically feasible trajectories for quadrotors using safe flight corridors in 3-d complex environments,” *IEEE Robotics and Automation Letters*, vol. 2, no. 3, pp. 1688–1695, 2017.
- [16] Z. Han, X. Huang, Z. Xu, J. Zhang, Y. Wu, M. Wang, T. Wu, and F. Gao, “Reactive aerobatic flight via reinforcement learning,” *arXiv preprint arXiv:2505.24396*, 2025.
- [17] G. Xu, T. Wu, Z. Wang, Q. Wang, and F. Gao, “Flying on point clouds with reinforcement learning,” *arXiv preprint arXiv:2503.00496*, 2025.
- [18] Z. Xu, X. Han, H. Shen, H. Jin, and K. Shimada, “Navrl: Learning safe flight in dynamic environments,” *IEEE Robotics and Automation Letters*, 2025.
- [19] G. Zhao, T. Wu, Y. Chen, and F. Gao, “Learning speed adaptation for flight in clutter,” *IEEE Robotics and Automation Letters*, vol. 9, no. 8, pp. 7222–7229, 2024.
- [20] Z. Han, L. Xu, L. Pei, and F. Gao, “Dynamically feasible trajectory generation with optimization-embedded networks for autonomous flight,” *IEEE Robotics and Automation Letters*, 2025.
- [21] J. Schulman, F. Wolski, P. Dhariwal, A. Radford, and O. Klimov, “Proximal policy optimization algorithms,” *CoRR*, vol. abs/1707.06347, 2017. [Online]. Available: <http://arxiv.org/abs/1707.06347>
- [22] Y. Song, A. Romero, M. Müller, V. Koltun, and D. Scaramuzza, “Reaching the limit in autonomous racing: Optimal control versus reinforcement learning,” *Science Robotics*, vol. 8, no. 82, p. eadg1462, 2023.
- [23] A. D. Ames, X. Xu, J. W. Grizzle, and P. Tabuada, “Control barrier function based quadratic programs for safety critical systems,” *IEEE Transactions on Automatic Control*, vol. 62, no. 8, pp. 3861–3876, 2016.
- [24] A. D. Ames, S. Coogan, M. Egerstedt, G. Notomista, K. Sreenath, and P. Tabuada, “Control barrier functions: Theory and applications,” in *2019 18th European control conference (ECC)*. Ieee, 2019, pp. 3420–3431.
- [25] R. Cheng, G. Orosz, R. M. Murray, and J. W. Burdick, “End-to-end safe reinforcement learning through barrier functions for safety-critical continuous control,” in *Proceedings of the AAAI Conference on Artificial Intelligence*, vol. 33, no. 01, 2019, pp. 3387–3395.
- [26] Xiao and Belta, “High-order control barrier functions,” *IEEE Transactions on Automatic Control*, vol. 67, no. 7, pp. 3655–3662, 2021.
- [27] M. Bertalmio, A. L. Bertozzi, and G. Sapiro, “Navier-stokes, fluid dynamics, and image and video inpainting,” in *Proceedings of the 2001 IEEE Computer Society Conference on Computer Vision and Pattern Recognition. CVPR 2001*, vol. 1. IEEE, 2001, pp. I–I.